

Magnetic order in the two-dimensional metal-organic framework manganese pyrazinecarboxylate with Mn-Mn dimers

S. Calder^{1,*}, R. Baral¹, N. Narayanan² and L. D. Sanjeeva^{2,3}

¹Neutron Scattering Division, Oak Ridge National Laboratory, Oak Ridge, Tennessee 37831, USA

²University of Missouri Research Reactor (MURR), University of Missouri, Columbia, Missouri 65211, USA

³Department of Chemistry, University of Missouri, Columbia, Missouri 65211, USA

(Received 29 September 2023; revised 8 November 2023; accepted 28 November 2023; published 15 December 2023)

The magnetic properties of $[\text{Mn}(\text{pyrazinecarboxylate})_2]_n$, empirical formula $\text{C}_{10}\text{H}_6\text{MnN}_4\text{O}_4$, are investigated through susceptibility, heat capacity, and neutron scattering measurements. The structure consists of Mn-Mn dimers linked on a distorted 2D hexagonal structure. The weak out-of-plane interactions create a quasi-2D magnetic material within the larger three-dimensional metal-organic framework structure. We show that this material undergoes a two-stage magnetic transition, related to the low dimensionality of the Mn lattice. First, at 5 K, which is assigned to the initial development of short-range order in the 2D layers. This is followed by long-range order at 3.3 K. Applied field measurements reveal the potential to induce magnetic transitions in moderately small fields of ~ 2 T. Neutron powder diffraction enabled the determination of a unique magnetic space group $P2_1'/c$ (No. 14.77) at 1.5 K. This magnetic structure consists of antiferromagnetically coupled Mn-Mn dimers with spins principally along the out-of-plane a axis.

DOI: [10.1103/PhysRevMaterials.7.124408](https://doi.org/10.1103/PhysRevMaterials.7.124408)

I. INTRODUCTION

Investigations of two-dimensional (2D) layered magnetic materials has revealed properties of interest for both fundamental and applied research. This is exemplified by graphene and beyond-graphene materials where the bulk compound has 2D layers weakly coupled through van der Waals bonding that can often be exfoliated or otherwise isolated down to a few or single layers [1–6]. In these inorganic compounds, numerous nontrivial topological and quantum behaviors have been observed and predicted due to the low dimensionality enhancing this behavior. Investigations on inorganic quasi-2D materials have uncovered topologically protected skyrmions [7,8], quantum spin liquids with emergent Majorana fermions [9], and spontaneous topological Hall effect [10]. Conversely, the tunability of coordination polymers or, equivalently, magnetic metal-organic frameworks (MOFs), offers a powerful but less explored material space to achieve analogous physics when magnetic metal ions are added to well-isolated 2D layered coordination structures [11–16]. An extremely large variety of structures are available through often highly predictable organic chemistry routes. The ability to control the in-plane 2D motif, the spacing of layers, and potential to introduce hybrid functionality on the organic linkers affords multiple intriguing research avenues for magnetic coordination polymers in the realm of quantum materials.

The material $[\text{Mn}(\text{pyrazinecarboxylate})_2]_n$, henceforth $\text{Mn}(2\text{-pzc})_2$, where 2-pzc = 2-pyrazinecarboxylate, contains well-isolated 2D layers of Mn^{2+} ions. Reference [17] previously reported on this material, with x-ray diffraction and

magnetic susceptibility measurements. The structure contains only one Mn site, however, the Mn ions within the layer have two distinct bonding environments with spacings of ~ 3.5 Å and ~ 5.6 Å. This results in Mn-Mn dimers that are linked to form a distorted 2D hexagonal network. These 2D layers are well isolated by an interlayer Mn-Mn distance of ~ 9.4 Å, with the bonding containing weak hydrogen bonds between ligands. $\text{Mn}(2\text{-pzc})_2$ is therefore expected to be a good realization of a quasi-2D material in a bulk compound. The previous powder magnetic susceptibility measurements were fit to a Curie-Weiss law down to 5 K and showed antiferromagnetic interactions with the Mn^{2+} ion in the $S = 5/2$ spin state. Inspecting the magnetic susceptibility in Ref. [17] reveals an apparent low-temperature anomaly, however, there was no discussion of any potential magnetic order transition.

Here we undertake magnetic susceptibility, heat capacity, and neutron powder diffraction measurements that reveal long-range magnetic order in $\text{Mn}(2\text{-pzc})_2$. The field-dependent behavior is investigated through single crystal magnetic susceptibility measurements that show a two-stage magnetic transition. In addition, there is a potential in-field magnetic transition, which indicates routes to tune the magnetic properties in moderate fields. Neutron powder diffraction is utilized to investigate the crystalline and magnetic structure through temperature-dependent measurements. Despite the presence of increased incoherent scattering from hydrogen in $\text{Mn}(2\text{-pzc})_2$, empirical formula $\text{C}_{10}\text{H}_6\text{MnN}_4\text{O}_4$, good quality neutron diffraction data are obtained. This highlights the strength of monochromatic high flux reactor-based neutron instruments coupled with the choice of large moment metal ions when investigating magnetic MOFs. At the lowest temperature of 1.5 K, long-range magnetic order is observed with several magnetic reflections identified. Symmetry

*caldersa@ornl.gov

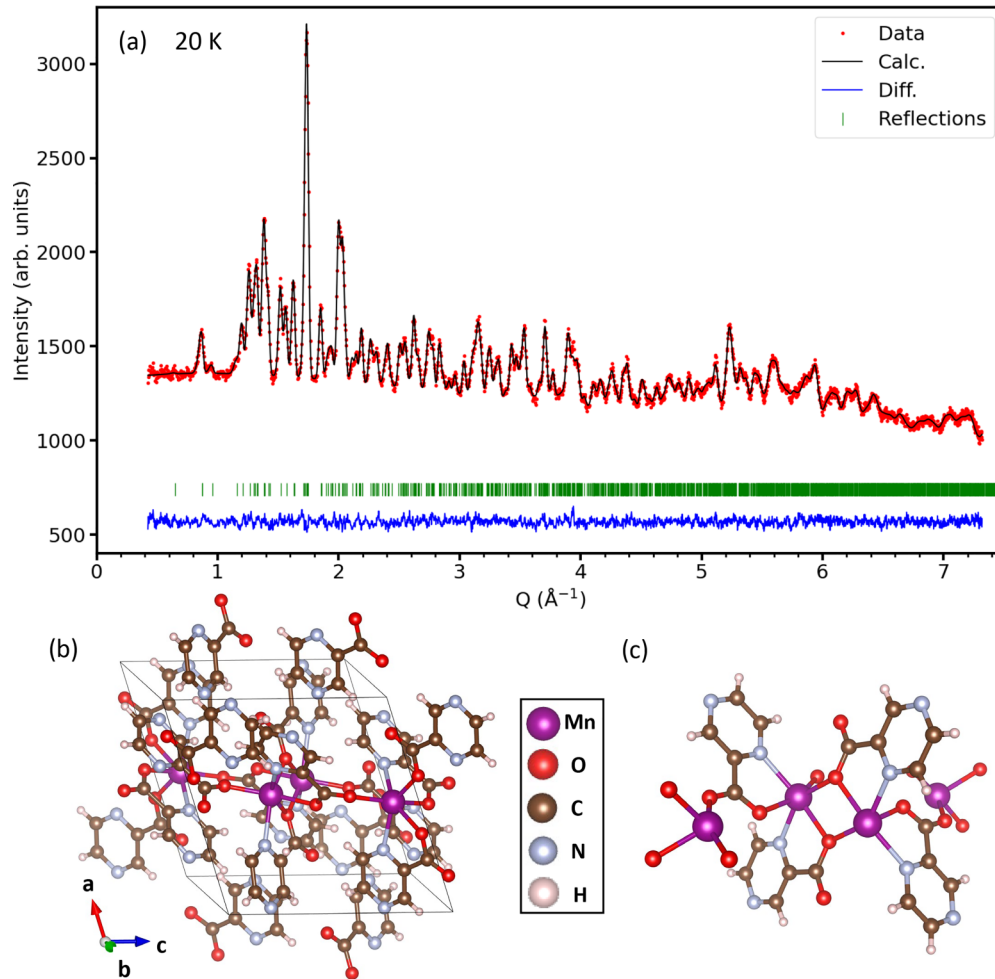


FIG. 1. (a) Rietveld refinement of neutron powder diffraction data for $\text{Mn}(2\text{-pzc})_2$ collected on the HB-2A instrument with a wavelength of 1.54 \AA at 20 K. (b) Crystal structure of $\text{Mn}(2\text{-pzc})_2$. The box represents the unit cell in the $P2_1/c$ space group. (c) Nearest- and next-nearest-neighbor Mn ions are bonded through distinct pathways of Mn-O-Mn and Mn-O-C-O-Mn.

analysis of this magnetic structure shows that the Mn-Mn dimers form antiferromagnetic pairs, with spins preferentially aligned in the out-of-plane a direction in the $P2_1'/c$ (No. 14.77) magnetic space group.

II. METHODS

A. Synthesis

Single crystals of $\text{Mn}(2\text{-pzc})_2$ were grown using the low-temperature hydrothermal method. First, a total of 0.37 grams of pyrazinecarboxylate acid ($\text{C}_5\text{H}_4\text{N}_2\text{O}_2$) and anhydrous manganese(II) acetate ($\text{Mn}(\text{CH}_3\text{COO})_2$) were mixed in a stoichiometric ratio of 2:1 with 5 mL of water and 5 mL of ethanol in a small beaker. The mixture was then mixed using a magnetic stirrer until everything was fully dissolved. Then the final mixture was loaded into a Teflon-lined stainless-steel autoclave, sealed well, and heated at 140°C for 12 h. After cooling to room temperature, a dark yellow solution was recovered and left to evaporate at room temperature. The $\text{Mn}(2\text{-pzc})_2$ crystals were formed during the solvent evaporation.

B. Magnetic property characterization

Temperature-dependent and field-dependent magnetic measurements were performed using a Quantum Design Magnetic Property Measurement System. Magnetic properties were determined using one single crystal with the weight of 3.8 mg. The single crystal specimen was affixed to a quartz rod using GE varnish and temperature-dependent magnetization measurements were carried out along three crystal directions. The temperature-dependent data were collected in the range of 2–350 K in an applied magnetic field up to 50 kOe. The anisotropic isothermal magnetization measurements were performed between 2–100 K in magnetic fields up to 60 kOe. The heat capacity (C_p) of the sample was measured using a physical property measurement system between 2–200 K under magnetic fields in the range 0–60 kOe. The crystal was placed on their flat surface on the heat capacity puck stage and the magnetic field was applied along the out-of-plane direction.

C. Neutron powder diffraction

Neutron powder diffraction measurements on five grams of undeuterated $\text{Mn}(2\text{-pzc})_2$ were carried out on the HB-2A

powder diffractometer at the High Flux Isotope Reactor, Oak Ridge National Laboratory [18,19]. Hydrogen-based materials present an extra challenge for neutron scattering by both adding to the neutron absorption and creating an increased background from incoherent scattering. These effects can be easier to account for with constant wavelength instruments due to the simpler data correction. Constant wavelength measurements were performed at 2.41 Å from the Ge(113) monochromator reflection and 1.54 Å from the Ge(115) reflection. The premono, presample, and predetector collimation was open-open-12'. A pyrolytic graphite filter was placed before the sample to remove higher order reflections for the 2.41 Å wavelength. The sample was contained in a 6-mm-diameter vanadium can and cooled in a liquid ^4He cryostat in the temperature range 1.5 K–300 K. The diffraction pattern was collected by scanning a 120° bank of 44 ^3He detectors in 0.05° steps to give 2θ coverage from 5° to 130°. Counting times were 8 h for the 2.41 Å measurements and 2 h for the 1.54 Å wavelength. Rietveld refinements were performed with FULLPROF [20]. Symmetry-allowed magnetic structures were considered using both representational analysis with SARAH [21] and magnetic space groups with the Bilbao Crystallographic Server [22]. Plots of the crystal and magnetic structure were prepared using VESTA [23].

III. RESULTS AND DISCUSSION

A. Crystal structure of $\text{Mn}(2\text{-pzc})_2$

We begin by considering the crystal structure of $\text{Mn}(2\text{-pzc})_2$, which was previously reported as being in the $P2_1/c$ space group [17]. To confirm this, we carried out neutron powder diffraction measurements in the paramagnetic regime of 20 K. The shorter wavelength of 1.54 Å was used to give the widest Q coverage to increase the number of measured reflections. Well resolved and strong nuclear Bragg peaks were observed. The data were refined with the reported $P2_1/c$ space group. Figure 1(a) shows the data and refinement. There is the expected elevated background, which is increased by a factor of ~ 6 for $\text{Mn}(2\text{-pzc})_2$ compared to measurements on a standard sample, with increased scattering at low Q that reduces as Q increases, as expected. We note that despite the presence of hydrogen, no additional treatment beyond that used for the majority of samples on HB-2A was required to model the background. For example, the data was readily accounted for by the usual straightforward 6 coefficient polynomial function used for most refinements of data on this neutron powder diffractometer (see Ref. [20] and the FULLPROF manual Eq. (3.4) for more details of standard backgrounds available). The refined lattice constants and atomic positions are given in Table I. Due to the large number of parameters, the thermal parameters were fixed to $B_{\text{iso}} = 0.3 \text{ \AA}^2$ during the analysis.

The structural unit cell is shown in Fig. 1(b). Considering the local Mn environment in Fig. 1(c) indicates two distinct bonding pathways. Nearest-neighbor bonds are Mn-O-Mn, which would suggest standard superexchange magnetic pathways, whereas the next-nearest-neighbor bonds are Mn-O-C-O-Mn, requiring extended superexchange magnetic interactions. The nearest-neighbor distance is 3.46(5) Å

TABLE I. Refined crystal structure parameters for $\text{Mn}(2\text{-pzc})_2$, empirical formula $\text{C}_{10}\text{H}_6\text{MnN}_4\text{O}_4$, at 20 K.

| Space group | $P2_1/c$ |
|----------------------|--|
| Lattice constants | $a = 10.2078(4) \text{ \AA}$ $b = 10.8444(4) \text{ \AA}$ $c = 10.1095(4) \text{ \AA}$ $\beta = 108.429(3)^\circ$ |
| Mn position and site | (0.498(3), 0.128(2), 1.101(3)) 4e |
| Goodness of fit | $\chi^2 = 1.72$, $R_{wp} = 8.80$ |

and the next-nearest neighbor is 5.71(3) Å. The Mn-Mn distance between the layers is 10.2078(5) Å and is mediated by a complex exchange pathway which includes weak hydrogen bonds. This creates the 2D layered structure of interest. Considering multiple unit cells, as shown in Fig. 2(a), highlights the well-isolated 2D network of Mn-Mn ions. The 2D network in the bc plane is shown in Fig. 2(b). The

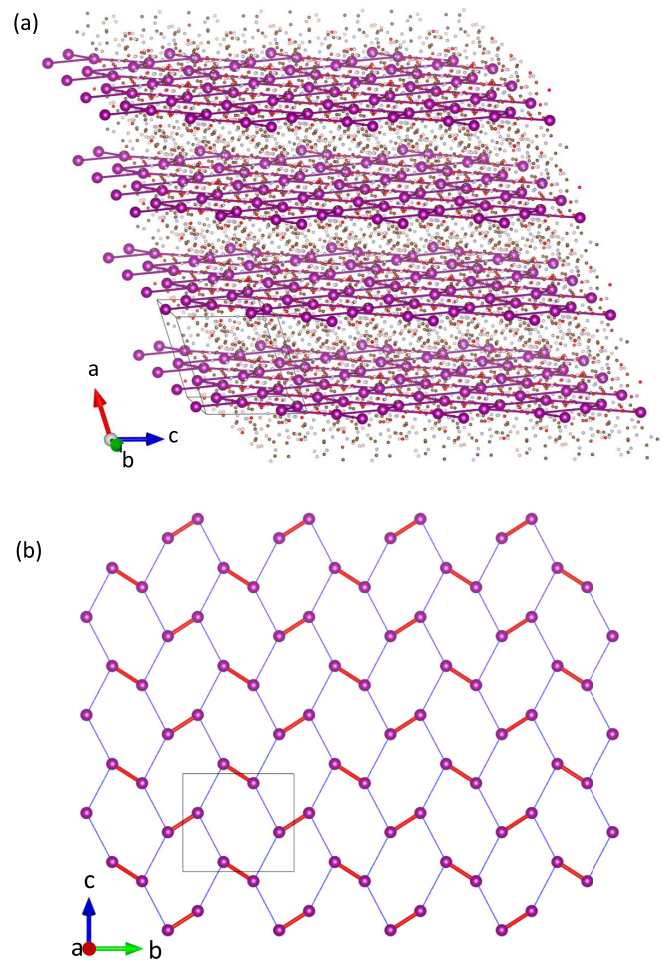


FIG. 2. (a) View of the 2D layers in $\text{Mn}(2\text{-pzc})_2$. (b) The nearest-neighbor dimers (thick red line) and next-nearest-neighbor (thin blue line) interactions within the 2D layers are shown between the Mn ions (purple sphere). The Mn ions form a distorted 2D honeycomb structure. The crystallographic unit cell is indicated by the grey box.

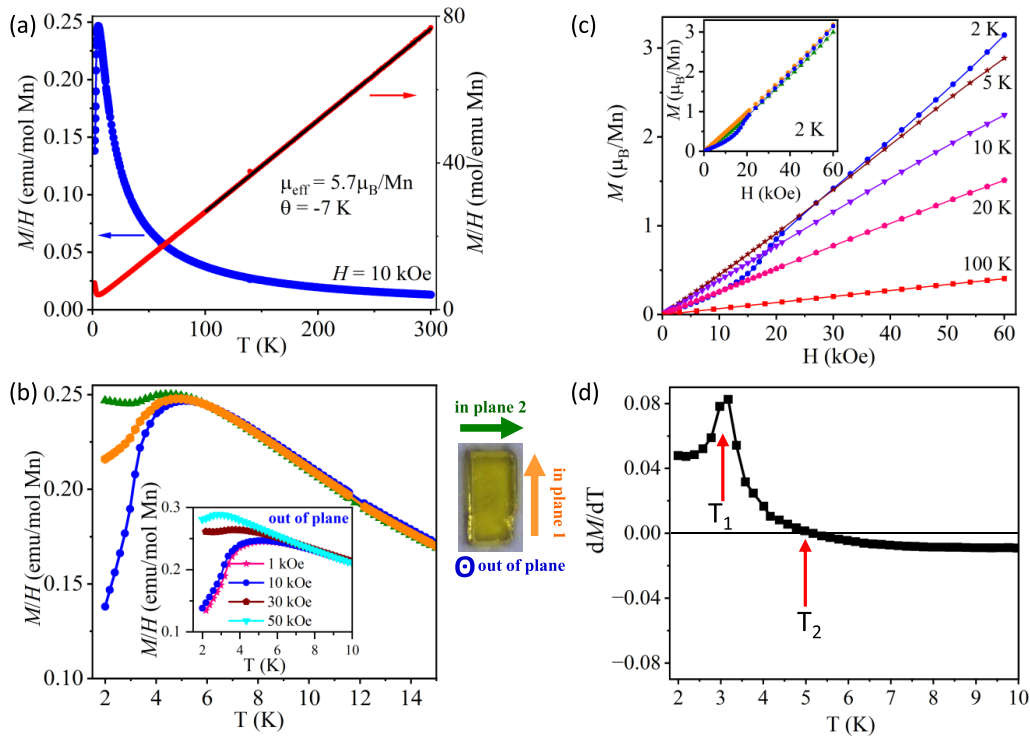


FIG. 3. (a) Magnetic susceptibility measurements from 2 K to 300 K. The solid black line is a fit using the Curie-Weiss law. (b) Directional dependent measurements showing a broad anomaly centered around 5 K. Green/yellow are in-plane and blue is out of plane. Measurements were in a 10 kOe field for all three directions. Inset: Out-of-plane magnetic field dependence. (c) Isothermal magnetization measurements for a field applied out of plane. Inset: Directional-dependent measurements at 2 K, where green/yellow are in plane and blue is out of plane. (d) Derivative of the susceptibility reveals two anomalies at 5 K and 3.2 K in a field of 10 kOe out of the plane.

nearest-neighbor Mn bonds can be viewed as Mn-Mn dimers which interact with the next-nearest-neighbor Mn ions to form a distorted 2D hexagonal layer.

B. Magnetic susceptibility and heat-capacity results

The initial report of $\text{Mn}(\text{2-pzc})_2$ in Ref. [17] measured magnetic susceptibility of a powder sample. Despite the apparent low-temperature anomaly recorded, no detailed discussion of potential magnetic ordering was reported. In the synthesis reported here, small $\text{Mn}(\text{2-pzc})_2$ crystals grew as rectangular rods, and we performed magnetic measurements in three orientations based on the crystal morphology as displayed in Fig. 3. The magnetic susceptibility produces a broad peak below 10 K with a maximum around 5 K. After that, it continuously decreases down to the lowest temperature measured of 2 K, indicating an antiferromagnetic transition. A broad transition is often a signature of short-range ordering associated with the layered nature of the structure. The inverse susceptibility was fitted using the Curie-Weiss law in the range of temperature $100 < T < 300$ K, see Fig. 3(a). This gives $\theta_{\text{CW}} = -7(1)$ K, indicating the antiferromagnetic nature of this compound. This is close to the long-range ordering temperature, discussed more below, and indicates a moderate frustration value of $f = \theta/T_N = 2$. This contrasts, for example, with a much higher frustration value of $f = 10$ found in certain triangular-based magnetic MOFs [24]. The effective magnetic moment from the fit was $\mu_{\text{eff}} = 5.7(2) \mu_B/\text{Mn}$,

which is comparable to the expected moment of a Mn^{2+} ion in the high-spin d^5 state of $5.9 \mu_B$.

The magnetic susceptibility data were also fit by taking only intradimer interactions into the account [25,26]. The fit to the 0.1 T data for the temperature range of 2 K–300 K gives an exchange interaction value of $J/k_B = -1.31(2)$ K ($J = -0.11$ meV). This is consistent with $\text{Mn}(\text{2-pzc})_2$ being comprised of weakly coupled antiferromagnetic dimers.

The magnetic susceptibility measured in different crystal orientations are displayed in Figs. 3(b) and 3(c). All field directions of in-plane and out-of-plane show a broad peak around the same temperature of 5 K at low fields ≤ 10 kOe. Increasing the field shifts the peak to lower temperatures. In general, the behavior under applied field is nontrivial with potentially a spin-flop transition which is further confirmed from our isothermal magnetization measurements in Fig. 3(c). This shows an anomaly at 2 K and 15 kOe. The inset of Fig. 3(c) showing directional dependent measurements indicates this anomaly occurs for fields applied out of plane only. Considering the derivative of susceptibility (dM/dT) indicates a two-stage transition at $T_2 = 5$ K and $T_1 = 3$ K see Fig. 3(d).

To gain further insights into the low-temperature behavior in $\text{Mn}(\text{2-pzc})_2$, we performed heat-capacity measurements. Figure 4 shows the results. The peak in the heat capacity for 0 T is observed at 3.3 K in Fig. 4(a). This is lower than the broad peak from magnetic susceptibility which occurs around 5 K, but consistent with the T_1 transition in the dM/dT

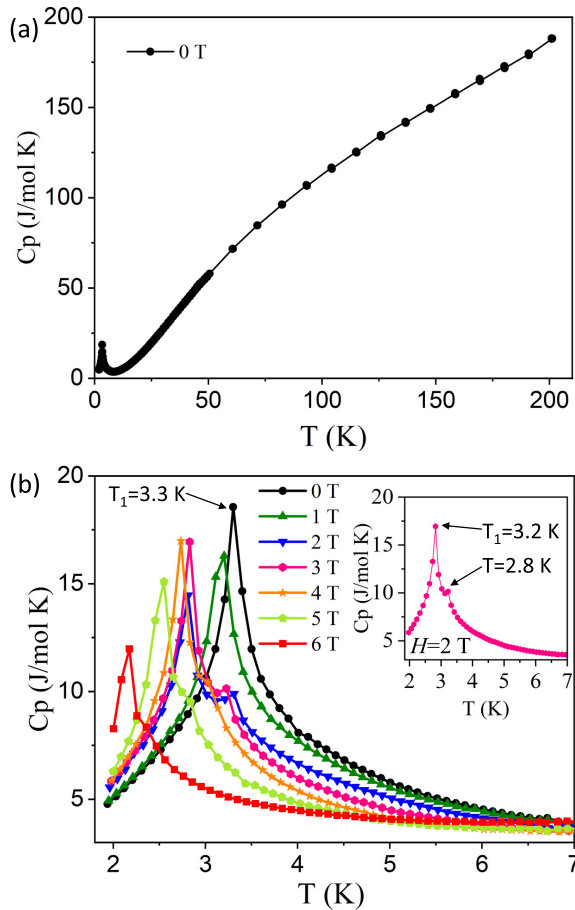


FIG. 4. (a) Zero-field heat capacity measurements on $\text{Mn}(2\text{-pzc})_2$ from 2 to 200 K. (b) Low-temperature and field-dependent heat-capacity measurements. The magnetic field was applied along the out-of-plane direction.

analysis. Applying a magnetic field leads to a lowering of the transition temperature in the heat-capacity measurements and the observation of a further transition in the form of a shoulder in the heat-capacity anomaly. This can be seen in the inset of Fig. 4(b) for a field of 3 T where a shoulder is measured at 3.2 K, followed by a further anomaly at 2.8 K. This anomaly at $T = 2.8$ K may indicate a further field-induced transition distinct from the T_1 and T_2 transitions.

Collectively, the susceptibility and heat-capacity results reveal multiple transitions that can be rationalized by considering the low-dimensional nature of $\text{Mn}(2\text{-pzc})_2$. We postulate that short-range order occurs around 5 K in the 2D layers. This gives the broad peak in the susceptibility rather than a sharp transition. Then, at 3.3 K the transition to three-dimensional long-range order occurs. This is observed in the heat capacity and also the magnetic susceptibility through dM/dT as a two-stage transition.

C. Magnetic structure of $\text{Mn}(2\text{-pzc})_2$

We now turn to neutron powder diffraction measurements to investigate the microscopic magnetic spin structure. Diffraction patterns were collected at 1.5 K and 20 K using the 2.41 Å wavelength, see Fig. 5(a). The high Q scattering

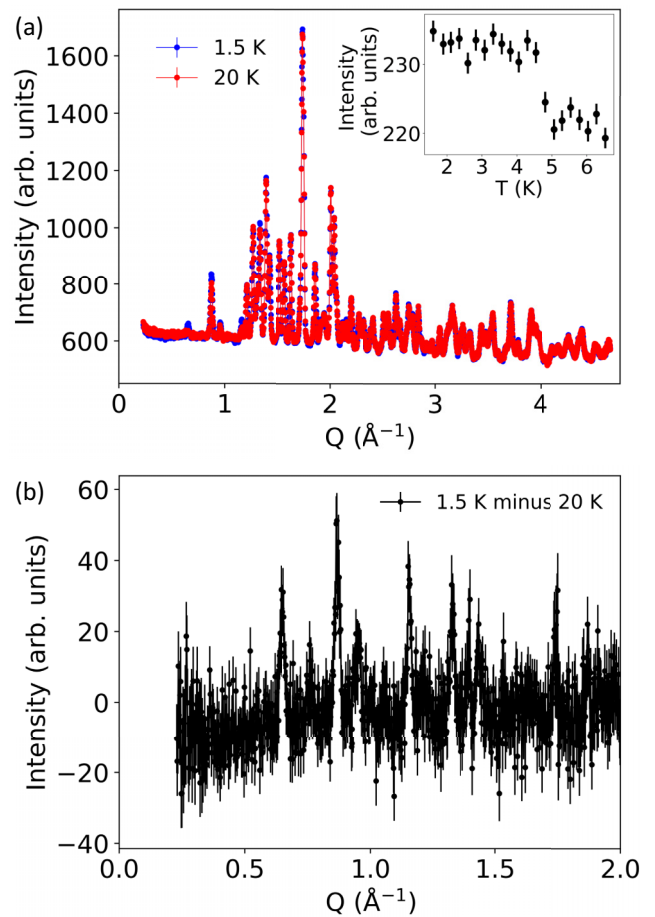


FIG. 5. (a) Neutron powder diffraction data collected at 1.5 K and 20 K. Inset: Intensity at $Q = 0.65 \text{ \AA}^{-1}$ as a function of temperature through the magnetic transition. (b) Difference of intensity at 1.5 K and 20 K in the powder diffraction data.

is unchanged, indicating no structural symmetry change. The low Q behavior below 2 \AA^{-1} , however, reveals additional intensity in the form of Bragg peaks. These can be assigned to magnetic ordering, with the width of the new magnetic peaks the same as the nuclear peaks, indicating long-range magnetic order at 1.5 K. The change in scattering is emphasized in the temperature difference plot in Fig. 5(b).

The intensity of the peak at $Q = 0.65 \text{ \AA}^{-1}$, which has no observable nuclear contribution at 20 K, was measured as a function of temperature to follow the onset of magnetic ordering, see inset Fig. 5(a). Increased scattering is observed at 5 K, which corresponds to the broad peak in magnetic susceptibility. This increases until it becomes saturated below 3 K. This measurement was exclusively of the intensity at $Q = 0.65 \text{ \AA}^{-1}$. It did not allow for a measurement of the peak width, therefore it is not possible to distinguish between short- or long-range order scattering. Since any diffuse scattering intensity will be small, it would be of interest for future studies to measure deuterated powder or larger single crystals to further investigate the potential short-range order in $\text{Mn}(2\text{-pzc})_2$ through this transition.

At 1.5 K, $\text{Mn}(2\text{-pzc})_2$ is in the long ranged magnetically ordered state. The measured magnetic Bragg peaks can all be indexed with a $\mathbf{k} = (0,0,0)$ propagation vector. Starting

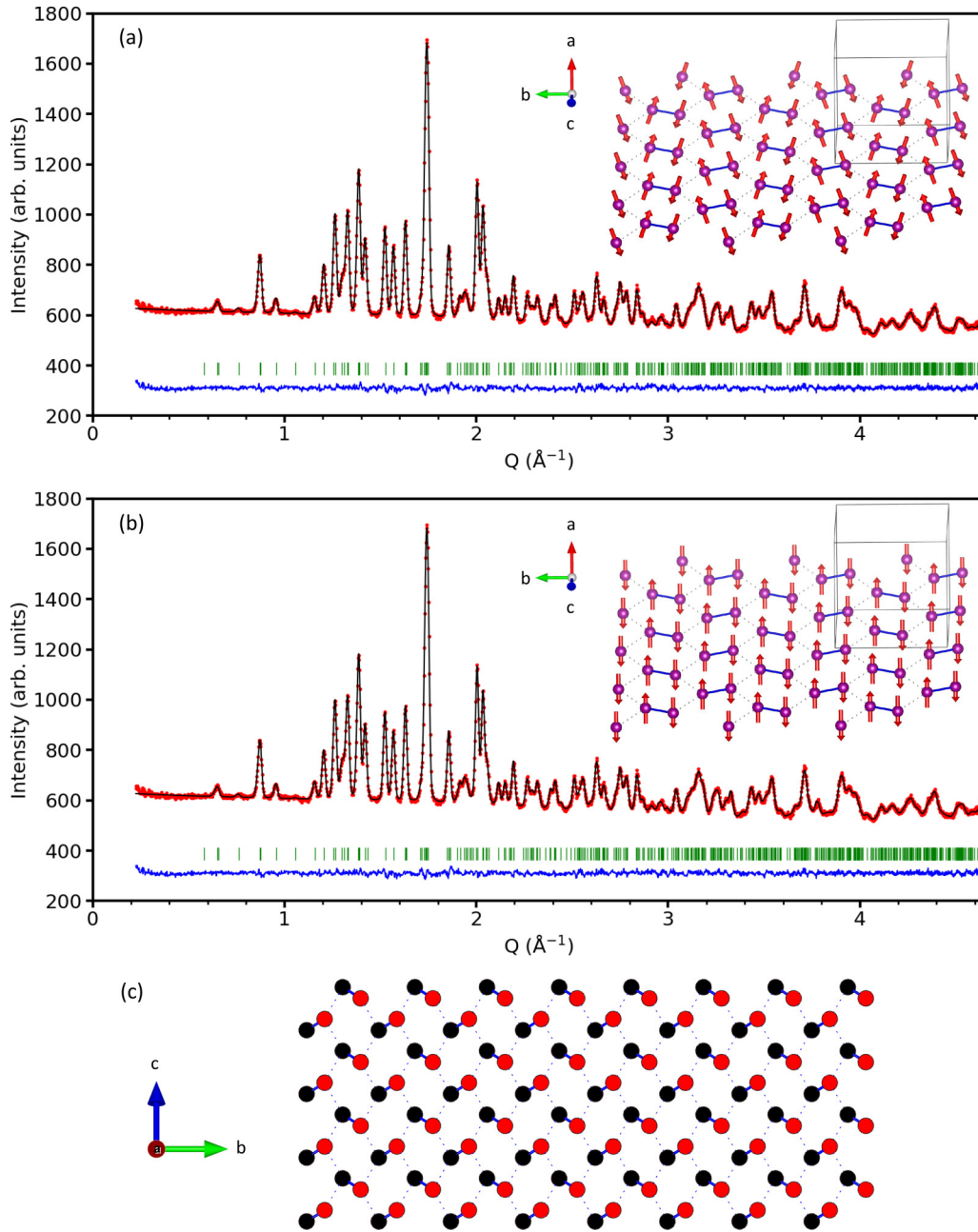


FIG. 6. Refinement of neutron powder diffraction data with $\lambda = 2.41 \text{ \AA}$ collected at 1.5 K using the magnetic space group $P2_1'/c$ with (a) moments along all $(\mathbf{m}_a, \mathbf{m}_b, \mathbf{m}_c)$ directions, (inset) magnetic structure, and (b) moments only along \mathbf{m}_a (inset) magnetic structure. The moments are shown as red arrows on the Mn ions, the nearest-neighbor dimer bonds are blue and the next-nearest-neighbor bonds are the dashed lines. The grey box represents the magnetic unit cell. (c) View of the 2D layers along the a axis. The red/black circles correspond to up/down spin directions on the Mn ion.

from the paramagnetic space group of $P2_1/c$ and using the determined propagation vector gives four irreducible representations (IRs) in a representational analysis approach or, equivalently, four maximal magnetic space groups. The magnetic space groups are $P2_1/c$ (No. 14.75), $P2_1'/c$ (No. 14.77), $P2_1/c'$ (No. 14.78), and $P2_1'/c'$ (No. 14.79). The corresponding IRs Γ_1 , Γ_2 , Γ_3 and Γ_4 , in Kovalevs representation, are shown in Table II and the basis vectors for these are in Table III.

For all candidate models, there are symmetry-allowed spin components along all crystallographic directions

$(\mathbf{m}_a, \mathbf{m}_b, \mathbf{m}_c)$. The data was refined against all four candidate magnetic models. Only magnetic space group $P2_1'/c$ (No. 14.77) (Γ_4) was able to reproduce the intensity of all observed magnetic reflections. Allowing the moments to refine freely gave $(\mathbf{m}_a, \mathbf{m}_b, \mathbf{m}_c) = (4.363(101), 1.261(562), 1.532(237))$ and total moment $4.3(2) \mu_B/\text{Mn}^{2+}$, which is reduced but nevertheless close to the full spin for a $S = 5/2$ ion of $5 \mu_B$. The refinement and corresponding spin structure are shown in Fig. 6(a), with $\chi^2 = 1.76$ and $R_{wp} = 6.15$. Confining the spins to only have a component along the a axis gives an equivalently good refinement, as can be seen in Fig. 6(b),

TABLE II. The point symmetry and magnetic space group for the space group $P2_1/c$ with $\mathbf{k} = (0, 0, 0)$. The decomposition of the magnetic representation for the Mn site (0.510, 0.134, 0.598) is $\Gamma_{\text{Mag}} = 3\Gamma_1^1 + 3\Gamma_2^1 + 3\Gamma_3^1 + 3\Gamma_4^1$.

| IR | BV | Point group | Magnetic space group | |
|------------|-------------|-------------|----------------------|-------------|
| Γ_1 | ψ_1 | $2/m$ | $P2_1/c$ | (No. 14.75) |
| | ψ_2 | $2/m$ | $P2_1/c$ | (No. 14.75) |
| | ψ_3 | $2/m$ | $P2_1/c$ | (No. 14.75) |
| Γ_2 | ψ_4 | $2/m$ | $P2_1/c'$ | (No. 14.78) |
| | ψ_5 | $2/m$ | $P2_1/c'$ | (No. 14.78) |
| | ψ_6 | $2/m$ | $P2_1/c'$ | (No. 14.78) |
| Γ_3 | ψ_7 | $2/m$ | $P2_1'/c'$ | (No. 14.79) |
| | ψ_8 | $2/m$ | $P2_1'/c'$ | (No. 14.79) |
| | ψ_9 | $2/m$ | $P2_1'/c'$ | (No. 14.79) |
| Γ_4 | ψ_{10} | $2/m$ | $P2_1'/c$ | (No. 14.77) |
| | ψ_{11} | $2/m$ | $P2_1'/c$ | (No. 14.77) |
| | ψ_{12} | $2/m$ | $P2_1'/c$ | (No. 14.77) |

with $\chi^2 = 1.75$ and $R_{wp} = 6.09$. The corresponding moment is slightly increased and closer to the full $S = 5/2$ values with $(m_a, m_b, m_c) = (4.47(9), 0, 0)$ and total moment $4.47(9) \mu_B/\text{Mn}^{2+}$. Allowing the spins to only be constrained to either the b or c axis could not fully account for the data. These results confirm the $S = 5/2$ nature of the Mn ion, however, the reduction in moment may be a consequence of the extended nature of the Mn-Mn exchange pathways leading to a degree of moment delocalization onto the surrounding ligands.

The spin behavior in the 2D layer can be visualized in Fig. 6(c). Black/red correspond to up/down Mn moments. The magnetic structure of $\text{Mn}(2\text{-pzc})_2$ has antiferromagnetic dimers of Mn-Mn ions. Each next nearest neighbor Mn-Mn interaction in the layer is also antiferromagnetic. Despite the

TABLE III. Basis vectors for the space group $P2_1/c$ with $\mathbf{k} = (0, 0, 0)$. The decomposition of the magnetic representation for the Mn site (0.510, 0.134, 0.598) is $\Gamma_{\text{Mag}} = 3\Gamma_1^1 + 3\Gamma_2^1 + 3\Gamma_3^1 + 3\Gamma_4^1$. The atoms of the nonprimitive basis are defined according to 1: (0.510, 0.134, 0.598); 2: (0.490, 0.634, 0.902); 3: (0.490, 0.866, .402); 4: (0.510, 0.366, 0.098).

| IR | BV | Atom | BV components | | |
|------------|-------------|------|-------------------|-------------------|-------------------|
| | | | $m_{\parallel a}$ | $m_{\parallel b}$ | $m_{\parallel c}$ |
| Γ_4 | ψ_{10} | 1 | 1 | 0 | 0 |
| | | 2 | 1 | 0 | 0 |
| | | 3 | -1 | 0 | 0 |
| | | 4 | -1 | 0 | 0 |
| | ψ_{11} | 1 | 0 | 1 | 0 |
| | | 2 | 0 | -1 | 0 |
| | | 3 | 0 | -1 | 0 |
| | | 4 | 0 | 1 | 0 |
| | ψ_{12} | 1 | 0 | 0 | 1 |
| | | 2 | 0 | 0 | 1 |
| | | 3 | 0 | 0 | -1 |
| | | 4 | 0 | 0 | -1 |

large Mn-Mn distance of $> 10 \text{ \AA}$ three-dimensional long-range order occurs, with the nearest neighbor Mn-Mn interlayer correlation being ferromagnetic. The large Mn moment of $S = 5/2$ is likely a driving factor in realizing long range order.

To induce further interesting behavior in $\text{Mn}(2\text{-pzc})_2$ and related materials, it will be of interest to reduce the moment size down to $S = 1/2$ to enhance quantum phenomena. This will be of particular interest with the dimer and 2D hexagonal layers that are hosts to exotic physics. As one example, the $\text{Mn}(2\text{-pzc})_2$ structure can be considered a distorted Shastry-Sutherland lattice [27,28]. Removing or controlling this distortion may provide routes to investigate this physics in MOFs and allow for a wider phase space of materials than the currently limited candidates.

IV. CONCLUSIONS

$\text{Mn}(2\text{-pzc})_2$ ($\text{C}_{10}\text{H}_6\text{MnN}_4\text{O}_4$) has been investigated with magnetic susceptibility, heat capacity, and neutron powder diffraction. The magnetic susceptibility and heat capacity collectively indicate development of short-range order at 5 K that proceeds the long-range magnetic phase transition at 3.2 K in zero field. The applied field measurements show anisotropic behavior with a field-driven anomaly above 2 T. Moreover, heat-capacity measurements in fields above 2 T reveal two observable anomalies with a small temperature window of ~ 0.5 K. Neutron powder diffraction was able to determine the magnetic structure in this undeuterated material. Following a symmetry analysis, only a single magnetic space group, $P2_1'/c$ (No. 14.77), was found to be consistent with the data. The analysis revealed the moments primarily aligned along the a axis, which is out of the 2D layers. These moments form antiferromagnetic dimers that are linked within a wider distorted hexagonal network. In general, the results show that coordination polymers or, equivalently, magnetic MOFs with both organic and inorganic building blocks offer unique material avenues to explore tailored structural motifs due to the versatility and predictability of organic chemistry.

ACKNOWLEDGMENTS

This research used resources at the High Flux Isotope Reactor, a DOE Office of Science User Facility operated by the Oak Ridge National Laboratory. This research used resources at the Missouri University Research Reactor (MURR). This paper was supported in part by a University of Missouri Research Council Grant (Grant No. URC-22-021). This paper has been partially supported by UT-Battelle, LLC under Contract No. DE-AC05-00OR22725 with the U.S. Department of Energy. The U.S. Government retains and the publisher, by accepting the paper for publication, acknowledges that the U.S. Government retains a nonexclusive, paid-up, irrevocable, worldwide license to publish or reproduce the published form of this paper, or allow others to do so, for U.S. Government purposes. The Department of Energy will provide public access to these results of federally sponsored research in accordance with the DOE Public Access Plan [29].

- [1] K. S. Novoselov, A. K. Geim, S. V. Morozov, D. Jiang, M. I. Katsnelson, I. V. Grigorieva, S. V. Dubonos, and A. A. Firsov, *Nature (London)* **438**, 197 (2005).
- [2] K. S. Novoselov, A. Mishchenko, A. Carvalho, and A. H. Castro Neto, *Science* **353**, aac9439 (2016).
- [3] M. Zeng, Y. Xiao, J. Liu, K. Yang, and L. Fu, *Chem. Rev.* **118**, 6236 (2018).
- [4] K. S. Burch, D. Mandrus, and J.-G. Park, *Nature (London)* **563**, 47 (2018).
- [5] B. Huang, M. A. McGuire, A. F. May, D. Xiao, P. Jarillo-Herrero, and X. Xu, *Nat. Mater.* **19**, 1276 (2020).
- [6] V. Baltz, A. Manchon, M. Tsoi, T. Moriyama, T. Ono, and Y. Tserkovnyak, *Rev. Mod. Phys.* **90**, 015005 (2018).
- [7] B. Ding, Z. Li, G. Xu, H. Li, Z. Hou, E. Liu, X. Xi, F. Xu, Y. Yao, and W. Wang, *Nano Lett.* **20**, 868 (2020).
- [8] T.-E. Park, L. Peng, J. Liang, A. Hallal, F. S. Yasin, X. Zhang, K. M. Song, S. J. Kim, K. Kim, M. Weigand, G. Schütz, S. Finizio, J. Raabe, K. Garcia, J. Xia, Y. Zhou, M. Ezawa, X. Liu, J. Chang, H. C. Koo *et al.*, *Phys. Rev. B* **103**, 104410 (2021).
- [9] A. Banerjee, J. Yan, J. Knolle, C. A. Bridges, M. B. Stone, M. D. Lumsden, D. G. Mandrus, D. A. Tennant, R. Moessner, and S. E. Nagler, *Science* **356**, 1055 (2017).
- [10] H. Takagi, R. Takagi, S. Minami, T. Nomoto, K. Ohishi, M. T. Suzuki, Y. Yanagi, M. Hirayama, N. D. Khanh, K. Karube, H. Saito, D. Hashizume, R. Kiyonagi, Y. Tokura, R. Arita, T. Nakajima, and S. Seki, *Nat. Phys.* **19**, 961 (2023).
- [11] Y.-Z. Zheng, Z. Zheng, and X.-M. Chen, *Coord. Chem. Rev.* **258-259**, 1 (2014).
- [12] P. A. Goddard, J. L. Manson, J. Singleton, I. Franke, T. Lancaster, A. J. Steele, S. J. Blundell, C. Baines, F. L. Pratt, R. D. McDonald, O. E. Ayala-Valenzuela, J. F. Corbey, H. I. Southerland, P. Sengupta, and J. A. Schlueter, *Phys. Rev. Lett.* **108**, 077208 (2012).
- [13] G. Mínguez Espallargas and E. Coronado, *Chem. Soc. Rev.* **47**, 533 (2018).
- [14] N. Stock and S. Biswas, *Chem. Rev.* **112**, 933 (2012).
- [15] P. J. Saines and N. C. Bristowe, *Dalton Trans.* **47**, 13257 (2018).
- [16] M. Kurmoo, *Chem. Soc. Rev.* **38**, 1353 (2009).
- [17] C. Cai, Y. Tian, X. Ren, Y. Li, X. You, and S. Li, *Trans. Metal Chem.* **27**, 924 (2002).
- [18] V. O. Garlea, B. C. Chakoumakos, S. A. Moore, G. B. Taylor, T. Chae, R. G. Maples, R. A. Riedel, G. W. Lynn, and D. L. Selby, *Appl. Phys. A* **99**, 531 (2010).
- [19] S. Calder, K. An, R. Boehler, C. R. Dela Cruz, M. D. Frontzek, M. Guthrie, B. Haberl, A. Huq, S. A. J. Kimber, J. Liu, J. J. Molaison, J. Neufeind, K. Page, A. M. dos Santos, K. M. Taddei, C. Tulk, and M. G. Tucker, *Rev. Sci. Instrum.* **89**, 092701 (2018).
- [20] J. Rodríguez-Carvajal, *Physica B: Condens. Matter* **192**, 55 (1993).
- [21] A. Wills, *Physica B: Condens. Matter* **276-278**, 680 (2000).
- [22] J. Perez-Mato, S. Gallego, E. Tasci, L. Elcoro, G. de la Flor, and M. Aroyo, *Annu. Rev. Mater. Res.* **45**, 217 (2015).
- [23] K. Momma and F. Izumi, *J. Appl. Crystallogr.* **44**, 1272 (2011).
- [24] J. M. Bulled, J. A. M. Paddison, A. Wildes, E. Lhotel, S. J. Cassidy, B. Pato-Doldán, L. C. Gómez-Aguirre, P. J. Saines, and A. L. Goodwin, *Phys. Rev. Lett.* **128**, 177201 (2022).
- [25] O. Kahn, *Molecular Magnetism* (VCH, New York, 1993).
- [26] G. Haselhorst, K. Wieghardt, S. Keller, and B. Schrader, *Inorg. Chem.* **32**, 520 (1993).
- [27] S. Miyahara and K. Ueda, *Phys. Rev. Lett.* **82**, 3701 (1999).
- [28] S. Haravifard, A. Banerjee, J. van Wezel, D. M. Silevitch, A. M. dos Santos, J. C. Lang, E. Kermarrec, G. Srajer, B. D. Gaulin, J. J. Molaison, H. A. Dabkowska, and T. F. Rosenbaum, *Proc. Natl. Acad. Sci. USA* **111**, 14372 (2014).
- [29] <http://energy.gov/downloads/doepublic-access-plan>.